Biomedicine & Pharmacotherapy 181 (2024) 117637

Contents lists available at ScienceDirect

Biomedicine & Pharmacotherapy

journal homepage: www.elsevier.com/locate/biopha

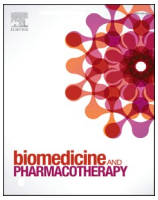

Plant-derived extracellular vesicles release combined with systemic DOX exhibits synergistic effects in 3D bioprinted triple-negative breast cancer

Lishan Cui [a,1], Giordano Perini [a,b,1], Antonio Minopoli [a], Alberto Augello [b,c], Marco De Spirito [a,b], Valentina Palmieri [a,b,c,*], Massimiliano Papi [a,b,*]

[a] Dipartimento di Neuroscienze, Università Cattolica del Sacro Cuore, Largo Francesco Vito 1, Rome 00168, Italy
[b] Fondazione Policlinico Universitario A. Gemelli IRCSS, Rome 00168, Italy
[c] Istituto dei Sistemi Complessi, CNR, Via dei Taurini 19, Rome 00185, Italy

ARTICLE INFO

Keywords:
3D bioprinting
scaffolds
hydrogel
local drug delivery, *Citrus limon L.* -derived extracellular vesicles
Triple negative breast cancer

ABSTRACT

Triple-negative breast cancer (TNBC) is a highly aggressive subtype of breast cancer, lacking targeted therapeutic options. Hydrogels, particularly gelatin methacrylate (GelMA), have emerged as promising materials for localized drug delivery due to their biocompatibility and tunable properties. This study investigates a dual-delivery system for enhancing the treatment efficacy of triple-negative breast cancer (TNBC) using a combination of extracellular vesicles (EVs) derived from *Citrus limon L.* and the chemotherapeutic drug doxorubicin (DOX). We fabricated 3D bioprinted GelMA scaffolds to achieve localized and controlled release of EVs and evaluated their synergistic effects with systemic DOX delivery on both primary and metastatic 3D TNBC models.

The GelMA scaffolds, especially those with 95 % methacrylation, exhibited higher stiffness, which enhanced their sustained release. Following 48-h incubation, the combination of EVs and DOX significantly increased cytotoxicity in the primary 3D TNBC model, reducing cell viability to approximately 30 % compared to controls. This was notably more effective than treatments with DOX or EVs alone. During the extended 7-day incubation period, the combination treatment continued to show superior efficacy, with persistently high levels of ROS generation and further reduction in cell viability. In a metastatic 3D TNBC model, a significant sensitivity to the combined treatment was observed, which notably inhibited aggregate formation and migration. Importantly, EVs-embedded scaffolds promoted the proliferation of human fibroblasts, highlighting their non-toxic nature, while concurrently inhibiting TNBC cell growth. This approach provides a promising strategy to improve the treatment outcomes of TNBC by exploiting the synergistic effects of local EVs release and systemic chemotherapy.

1. Introduction

Triple-negative breast cancer (TNBC) accounts for 15–20 % of all breast cancer cases and is known for its highly aggressive clinical behavior. This subtype of breast cancer is characterized by the lack of expression of estrogen receptors, progesterone receptors, and human epidermal growth factor receptor 2 HER2/neu (HER2). The absence of these receptors precludes the use of hormonal therapies, (such as tamoxifen or aromatase inhibitors) or targeted therapy (e.g., trastuzumab), posing a significant treatment challenge and positioning chemotherapy as the mainstay of treatment [1]. Doxorubicin (DOX), also known as Adriamycin, is an anthracycline antibiotic that is widely used

Abbreviations: AFM, Atomic force microscopy; BCA, Bicinchoninic acid; BCS, Breast-conserving surgery; CAD, Computer-aided design; CLEVs, *Citrus limon L.*-derived EVs; DAPI, 4',6-Diamidino-2-Phenylindole; DMEM, Dulbecco's Modified Essential Medium; DOX, Doxorubicin; DOX·HCl, Doxorubicin hydrochloride; ECM, extracellular matrix; EVs, Extracellular vesicles; FBS, Fetal bovine serum; GelMA, Gelatin methacrylate; GFR, Growth Factor Reduced; H_2DCFDA, Fluorinated derivative of 2′,7′-dichlorofluorescein; HER2, Human epidermal growth factor receptor 2 HER2/neu; IC50, The half-maximal inhibitory concentration; LAP, Lithography-based additive manufacturing; LI, Light intensity; MMP, Matrix metalloproteinase; MSCs, mesenchymal stem cells; NTA, Nanoparticle tracking analysis; PBS, Phosphate-buffered saline; RGD, Arginyl-glycyl-aspartic acid; ROS, Reactive oxygen species; RPMI, Roswell Park Memorial Institute; TNBC, Triple-negative breast cancer; TEM, Transmission electron microscopy.

* Corresponding authors at: Dipartimento di Neuroscienze, Università Cattolica del Sacro Cuore, Largo Francesco Vito 1, Rome 00168, Italy.
E-mail addresses: valentina.palmieri@cnr.it (V. Palmieri), massimiliano.papi@unicatt.it (M. Papi).

[1] These authors contributed equally

https://doi.org/10.1016/j.biopha.2024.117637
Received 7 August 2024; Received in revised form 25 October 2024; Accepted 28 October 2024
Available online 30 October 2024

in systemic cancer treatment, including TNBC. However, its efficacy is often limited by systemic toxicity and the development of drug resistance. The choice of a systemic treatment can improve cancer operability or enable breast-conserving surgery (BCS) [2]. Prospective trials on the oncologic safety of BCS combined with neoadjuvant therapy defined acceptable low local recurrence rates if negative surgical margins can be obtained. However, the significant risk of missing residual disease may preclude future adoption of this approach [3].

The local therapy strategy for breast cancer has gained significant attention due to its advantage of delivery high concentrations of therapeutic agents directly to tumor sites, allowing for controllable and sustained release. Among the various delivery systems available, hydrogels stand out as ideal platforms for local therapy. Hydrogels are hydrophilic gels with a three-dimensional network structure with physical and mechanical properties easily tailored by adjusting the types and molecular weights of the polymers, the extent of crosslinking during gelation, or through specific fabrication technologies. Additionally, their typical interporous structure provides ample space to encapsulate various agents with high efficiency [4–6]. Hydrogels can be classified into natural and synthetic categories [7]. Natural hydrogels, derived from biological substances like polysaccharides and proteins, offer excellent biocompatibility and ECM-like functions that support cell growth and differentiation. However, they often lack stability and mechanical strength. Synthetic hydrogels, on the other hand, provide better mechanical properties but lack the biological activity inherent to natural hydrogels [8]. Advances in technology have led to the development of various specialized hydrogels, including stimulus-responsive [9], self-healing injectable [10], strongly adhesive and conductive hydrogels [11]. These innovations have expanded the potential applications of hydrogels in tumor therapy. [12].

Gelatin methacrylate (GelMA) is a hydrogel derived from gelatin that has been chemically modified with methacrylic anhydride [13]. GelMA retains the bioactive sequences of gelatin, such as the arginyl-glycyl-aspartic acid (RGD) motifs and matrix metalloproteinase (MMP)-sensitive sites, which facilitate cell adhesion, proliferation, and remodeling [14]. GelMA hydrogels are notable for their tunable mechanical properties, which can be adjusted by altering the degree of methacrylation or polymer concentration. This tunability allows for the customization of GelMA hydrogels to suit specific tissue engineering applications. One of the significant advantages of GelMA is its ability to support the encapsulation and controlled release of therapeutic agents, such as extracellular vesicles (EVs) [15], protecting EVs from degradation and denaturation, maintaining their stability and functional properties. EVs are membrane-bound nano-sized particles secreted by various cell types [16] with the function of intercellular communication. In cancer therapy, EVs offer a promising approach due to their ability to deliver therapeutic molecules directly to tumor cells, thereby reducing off-target effects and enhancing treatment specificity [17]. The therapeutic potential of EVs is driven by their bioactive cargo, including proteins, lipids, and nucleic acids, which collectively contribute to their anticancer efficacy.

In our previous study, we demonstrated that *Citrus limon L.*-derived EVs (CLEVs) exhibited anticancer effects on TNBC by inhibiting the phosphorylation of key proteins in the PI3K/AKT and MAPK/ERK signaling pathways, which are essential for cancer cell proliferation, survival, and metastasis [18]. Plant-derived EVs, such as those from *Citrus limon L.*, have shown superior biocompatibility, safety, and ease of production, leading to their increased use in therapeutic applications [19]. In contrast, mammalian cell-derived EVs, notably from mesenchymal stem cells (MSCs), face challenges including immune rejection and limitations in large-scale production. A major concern is the potential transmission of deleterious genetic abnormalities, infections, or undesirable traits from donor cells to EVs, which could adversely affect the recipient, especially cancer patients whose cells may have undergone malignant transformation. During tumor progression, bone marrow-derived MSCs exhibit tumor tropism, responding to chemokine gradients and migrating to the tumor microenvironment (TME) [20,21]. To mitigate the risks associated with mammalian cell-derived EVs, we opted for *Citrus limon L.*-derived EVs as a natural, safer alternative. We hypothesize that combining a local therapy based on CLEVs-loaded hydrogels, with systemic DOX chemotherapy presents a synergistic strategy to enhance the overall efficacy adjuvant therapy, reduce side effects, and improve patient outcomes in breast conservation surgery. In this study, we combined the local delivery of from GelMA scaffolds with systemic delivery of DOX to target a 3D TNBC model. We incorporate the CLEVs into GelMA scaffolds to analyze controlled release system for EVs in different spatial arrangement of tumor cells obtained by bioprinting technology. This allowed as to simulate local positive margins of micrometastases or isolated cells treatment. This dual-delivery strategy addresses the limitations of conventional therapies and markedly improves therapeutic outcomes.

2. Materials and methods

2.1. Isolation and characterization of EVs derived from Citrus limon L.

The isolation and characterization of EVs derived from *Citrus limon L.* juice followed methods outlined previously [18]. Briefly, *Citrus limon L.* juice underwent sequential centrifugation using a 30 % sucrose/D2O cushion ultracentrifugation method. Ultracentrifugation was performed with a Type 50.2 Ti fixed-angle rotor (Beckman Coulter Inc., Brea, CA, USA). The morphology and the size were verified by transmission electron microscopy (TEM). The concentration and size distribution of EVs were assessed by nanoparticle tracking analysis (NTA) using the NanoSight NS300 (Malvern Technologies, Malvern, UK). The capture settings are as follows: Camera Type is sCMOS, Laser Type is Blue 488, the camera level is set to 16, and the detection threshold is set to 5. The protein concentrations of EVs were measured by BCA quantification assay, using the bicinchoninic acid (BCA) assay kit (Thermo Fisher Scientific, Waltham, MA), following the manufacturer's instructions.

2.2. 3D Bioprinting of EVs-embedded 3D Scaffolds

PhotoGel-INK ~95 % DOM (Type A, 300 Bloom, Porcine Gelatin, Cat No. # 5208; California, USA) and PhotoGel-INK ~50 % DOM (Type A, 300 Bloom) were purchased from Advanced BioMatrix, Carlsbad, CA. The gels were pre-warmed at 37°C for 30 min before use. Bioinks were diluted in 0.22 μm filtered PBS (1X) to reach the final concentration of 5 % w/v with 0.25 % LAP. The 3D scaffolds were printed by using BIONOVA X 3D bioprinter (CELLINK, Boston, MA, USA), at room temperature. The structure of scaffolds was designed by using 3D computer graphics and computer-aided design (CAD) application software Rhinoceros (Robert McNeel &Associates). The 3D models were designed as a cubic scaffold with dimensions of 5 ×5×1 mm (X, Y, Z) and internal micro-grid patterns of 0.1 mm, 0.5 mm, and infill, respectively. The scaffold featured a hierarchical structure consisting of ten layers, divided into three sections. The initial section featured a motion speed of 0.005 mm/s alongside a section height of 0.05 mm. The second section featured a motion speed of 0.05 mm/s, along with an increased section height of 0.9 mm. Lastly, the third section ran at a motion speed of 0.003 mm/s, with a section height of 0.05 mm. Before starting bioprinting, the BIONOVA X printer was sterilized with UV light for 15 min. 10^8 particles of EVs incorporated with 50 % and 95 % methacrylated gelatin bioinks were applied to the 24-well Glass Bottom Plate, Type 1 (Non-Adhesive) (Cat. No: D16110025299). The scaffolds were crosslinked using UV light at a wavelength of 405 nm with light intensities of 4, 8, and 16 mW/cm^2, corresponding to three distinct intensity levels of 50 %, 75 %, and 100 %.

2.3. Atomic force microscopy (AFM)

The stiffness (Young's modulus, E) of two scaffolds fabricated by

50 % and 95 % methacrylated gelatin were detected by IT-AFM (Nanowizard II, JPK Instruments) analysis. The scaffolds were secured to a plastic Petri dish with glue to stabilize them and prevent movement during measurements. MikroMasch CSC-38/No Al silicon cantilevers with a tip radius of about 8 nm and a nominal spring constant of 0.05 N/m were used for the measurements. The cantilever spring constant was precisely determined by thermal calibration before each measurement. Force curves were acquired by using an indentation force of 4 nN at indentation speed 2 μm/s. The data were analyzed by fitting each force distance curve, with the JPK SPM data processing software, using the Hertz/Sneddon model type for conical indenters [22]. Cone tip shape with half-cone angle 20° for the exploited tips, passion ratio 0.5.

2.4. Quantification of EVs Release from 3D scaffolds

The release profile of EVs from the 3D scaffolds was monitored over a period of 7 days. Prior to the bioprinting process, EVs were initially labeled with Calcein-AM. In detail, EVs were incubated with Calcein-AM for 30 min at 37°C, followed by ultracentrifugation at 100,000 x g for 1 h. The resulting pellet was then resuspended in 100 μL of PBS. The EVs-embedded scaffolds were bioprinted onto a 24-well Glass Bottom Plate and subsequently immersed in 1 mL of PBS to facilitate monitoring of their release. Prior to measurements, the plate was gently shaken in an orbital motion for 10 s, and the release of EVs was monitored over a period of up to 7 days. The fluorescence intensities were quantified by using Cytation3 Cell Imaging Multi-Mode Reader (BioTek, Winooski, VT, USA) with excitation at 488 nm and emission recorded at 525 nm.

2.5. Cell culture in 2D

Human basal-like TNBC cell line HCC-1806 and human fibroblasts were purchased from American Type Culture Collection (ATCC, Rockville, MD, USA). Fibroblasts were maintained in culture in Dulbecco's Modified Essential Medium (DMEM, Sigma-Aldrich, St. Louis, MO, USA) enriched with 10 % fetal bovine serum (FBS, Gibco, Life Technologies) and 2 % penicillin–streptomycin (Sigma-Aldrich, St. Louis, MO, USA), while HCC-1806 was cultured in Roswell Park Memorial Institute (RPMI) 1640 medium (Thermo Fisher Scientific, Waltham, MA, USA) supplemented with the same concentrations of fetal bovine serum and penicillin–streptomycin. The cells and maintained at 37 °C with 5 % CO_2 under a humidified atmosphere.

2.6. Cellular Uptake of EVs and DOX

EVs were labeled using Calcein-AM as previously described [18]. HCC-1806 cells were seeded at a density of 1 $\times 10^4$ cells per well in an 8-well chambered coverglass (Cellvis, Cat. #: C8–1.5-H-N). The day after, cells were incubated with Calcein-AM labeled-EVs alone, Doxorubicin hydrochloride (DOX·HCl) alone, or a combination of EVs and DOX (EVs+DOX) for 24 h at 37°C. After labelling, the cells were fixed with 4 % paraformaldehyde for 20 min at room temperature, and then washed two times with PBS. Fixed cells were permeabilized with 0.1 % Triton™ X-100 (Sigma-Aldrich) for 15 min at RT, followed by two washes with PBS. Subsequently, the nucleus was incubated with DAPI (4′,6-Diamidino-2-Phenylindole) for 15 min in the dark condition at room temperature. The cellular uptake of EVs, DOX, and EVs+DOX was observed using confocal microscopy. Fluorescence images were acquired using Nikon's A1 MP+ multiphoton confocal microscope, equipped with a 60X oil immersion objective.

2.7. 3D bioprinting of TNBC model in matrigel

The CELLINK BIO X 3D Bioprinter was employed to bioprint 10,000 cells per drop in the Corning Matrigel Growth Factor Reduced (GFR) Basement Membrane Matrix (Cat No. # 354230). The Matrigel was thawed overnight in a 4°C refrigerator before use. Cells were trypsinized and resuspended in pre-chilled culture medium after centrifugation and then mixed with Matrigel to reach 8 mg/mL. The cell-laden Matrigel suspension was loaded into printing cartridges pre-cooled on ice, which were mounted on the cooled printhead of a CELLINK BIO X 3D Bioprinter. The print bed temperature was pre-set to 37°C, while the printhead temperature was set to 4°C. The extrusion rate was maintained at 5 μL/s, with a volume of 5 μL. The height of the Z-lift between wells was set to 2.0 mm. After printing, the 48-well plate containing the droplets was inverted and incubated at 37°C for 20 min to facilitate polymerization. Subsequently, 300 μL of culture medium was added to each well.

2.8. CellTiter-Glo 3D cell viability assay

Cell viability of the 3D models was assessed using the CellTiter-Glo 3D Luminescent Cell Viability Assay (Promega, Madison, WI, USA). The CellTiter-Glo 3D Reagent effectively penetrates spheroids, enabling accurate determination of 3D cytotoxicity. The 3D bioprinted TNBC models were filled with complete RPMI medium and incubated overnight at 37°C with 5 % CO_2. The day after, the 3D model was subjected to various treatments for durations of 48 h or 7 days at 37°C. Post-incubation, cells were gently washed with PBS. Subsequently, an equal volume of CellTiter-Glo 3D reagent was added to each well of the cell culture plate, and the plate was agitated for 5 min to induce cell lysis, followed by a 25-min incubation at room temperature in darkness to stabilize the luminescence signal. Luminescence intensities were observed using the Cytation3.

2.9. Cellular reactive oxygen species (ROS) detection assay

The fluorinated derivative of 2′,7′-dichlorofluorescein (H_2DCFDA; Sigma-Aldrich) was used to detect ROS generation in the 3D TNBC model. Droplets containing 10,000 cells in 5 μL of Matrigel were printed into 48-well plates. The day after, the cells were treated and then incubated at 37°C for either 48 h or 7 days. After incubation, cells were carefully washed with PBS, and 300 μL of H_2DCFDA at a final concentration of 10 μM was added to the wells, and incubated at 37°C for 30 min. After incubation, the cells were carefully washed with PBS and 300 μL of H_2DCFDA at a final concentration of 10 μM was added to the wells and incubated at 37°C for 30 min. Subsequently, the reagents were removed and replaced with culture medium in preparation for ROS detection. The fluorescence intensities were measured using a Cytation 3 Cell Imaging Multi-Mode Reader (BioTek, Winooski, VT, USA) with excitation at 495 nm and emission at 525 nm. The ROS levels generated after treatment were normalized to the number of viable cells.

2.10. Cell adhesion assay

The scaffolds with or without 10^8 particles of EVs were bioprinted using a BIONOVA X bioprinter into a 24-well Glass Bottom Plate. A total of 1 $\times$ 10^5 HCC-1806 cells and fibroblasts were seeded onto the scaffolds. After 48 h of incubation at 37°C, the cells were labelled with 5 μM Calcein-AM for 20 min at 37°C. Subsequently, the cells were washed with PBS and stained with 10 μM DAPI for 10 min in the dark at room temperature. Fluorescence images were acquired with Cytation 3 Cell Imaging Multi-Mode Reader in blue (excitation 350 nm, emission 460 nm) and green (excitation 495 nm, emission 525 nm) channels after careful washing to remove not attached cells.

2.11. Wound healing assay

A density of 10^5 fibroblasts was plated in a 24-well plate and incubated overnight at 37°C in a 5 % CO_2 incubator. The following day, when the cells reached approximately 90 % confluence, the cell monolayers were scratched using a sterile P-200 pipette tip. They were then washed twice with PBS to eliminate floating cells and debris. PBS was

pre-warmed to 37°C to prevent cell detachment during the washing process. Subsequently, cells were incubated for 48 h with either no treatment, the scaffold alone (S (-) EVs), or the scaffold embedded with 10^8 particles of EVs (S (+) EVs). Wound healing progress was continuously monitored at specified time points using the Cytation 3 Cell Imaging Multi-Mode Reader at 4X magnification. The wound closure area was quantified using ImageJ software.

2.12. Statistical analysis

Quantitative data derived from three independent experiments are presented as means ± SEM. Statistical significance was assessed using one-way ANOVA and two-way ANOVA, followed by Tukey's multiple comparison post-hoc test. Statistical analysis was performed using GraphPad Prism9 software (San Diego, CA, USA), and the significance level was set at $p < 0.05$ (*$p < 0.05$; **$p < 0.01$; ***$p < 0.001$; ****$p < 0.0001$).

3. Results

3.1. Fabrication and characterization of 3D GelMA scaffold-based patches

We 3D-bioprinted hydrogel-based, micropatterned scaffold patches

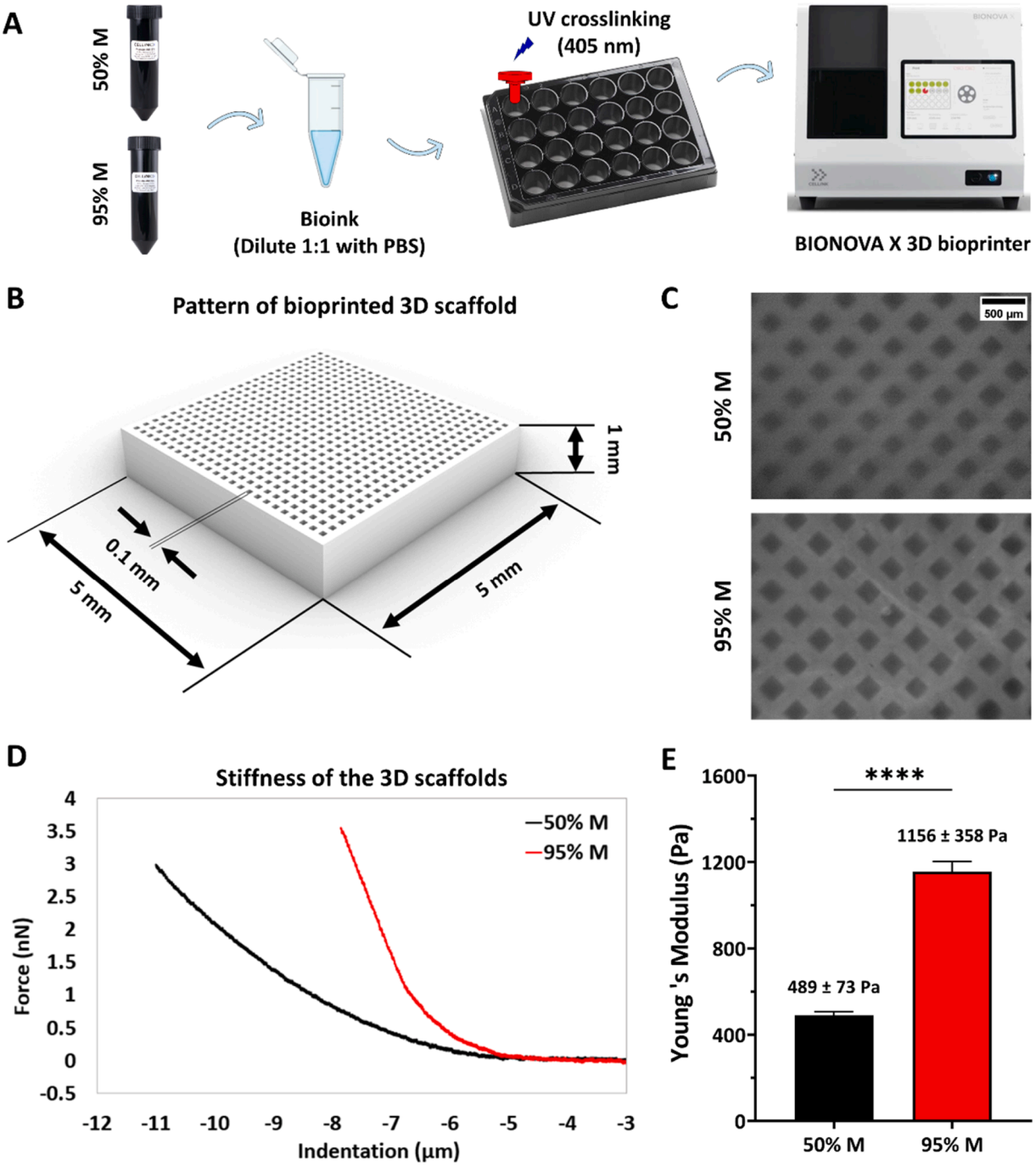

Fig. 1. Fabrication and characterization of bioprinted 3D scaffolds. **(A)** Schematic illustration of 3D bioprinting of the scaffolds. **(B)** 3D computer graphics micropatterning of the scaffold. **(C)** The patterns of 3D scaffolds fabricated using 50 % M and 95 % M PhotoGels were observed with 4X magnification using a Cytation 3 (Scale bar = 100 µm). **(D)** Representative AFM results of stiffness measurements. **(E)** Compressive Young's modulus of 50 % M and 95 % M scaffolds.

to achieve localized release of EVs (Fig. 1A) using GelMA hydrogel, also known as photo-crosslinkable gelatin, that was selected for its exceptional biocompatibility and moldability. The scaffold structure was designed utilizing advanced 3D computer-aided design (CAD) software, with dimensions of 5 mm in length and width, and a height of 1 mm, infilled with 0.1 mm cube squares (Fig. 1B). Two different degrees of methacrylated gelatin, 50 % and 95 %, were employed for fabrication of the scaffold patch and crosslinked by using recommended UV light intensities of 75 % (i.e., 8 mW/cm^2). As shown in Fig. 1C, well-distributed grid structures with precisely arranged internal squares were obtained.

The mechanical properties of the scaffolds were evaluated by measuring their stiffness using AFM. Force-distance curves were acquired to determine the Young's Modulus of the scaffolds fabricated with 50 % and 95 % methacrylated gelatin (Fig. 1D). The analysis revealed that the scaffolds made with 95 % methacrylated gelatin exhibited a significantly higher stiffness, with a Young's Modulus twice that of the scaffolds made with 50 % methacrylated gelatin (Fig. 1E). This increase in stiffness is attributed to the higher degree of methacrylation, which enhances the crosslinking density within the hydrogel matrix, thereby improving its mechanical strength.

3.2. Controlled release of EVs from 3D-printed micropatterned GelMA patch

In our previous research, we demonstrated that *Citrus limon L.*-derived EVs have potent anticancer effects on TNBC cells. To retain their biological functions and to achieve their controlled release, embedding EVs in hydrogels is an effective approach as part of a composite system [23,24]. To investigate the release kinetics of EVs from GelMA scaffolds and identify critical fabrication factors influencing their release, we embedded EVs into the scaffolds and analyzed their release profiles. Fig. 2A shows a schematic diagram of EVs characterization and release from the scaffolds. EVs were obtained from *Citrus limon L.* using a sucrose-based ultracentrifugation method, achieving high-quality, large-scale production of EVs. The average diameter of isolated EVs was approximately 100 nm (Fig. 2B), and the nanovesicle concentration ranged from 1.38e+09 +/- 2.09e+08 particles/mL (Fig. 2C). EVs were fluorescently labeled with Calcein-AM and embedded in scaffolds having different stiffness fabricated using 50 % and 95 % methacrylate gelatin bioinks, respectively. Bioprinting was performed using a high-precision BIONOVA X Bioprinter to create scaffolds with a well-defined architecture featuring a 0.1 mm cubic infilled mesh grids to facilitate controlled spatial distribution. Considering that the light intensity (LI) used for cross-linking may significantly affect the retention and release of EVs, the scaffolds were cross-linked at three different light intensities — 50 %, 75 %, or 100 %, to figure out the optimal cross-linking conditions. The drug release efficiency of EVs-embedded scaffolds was monitored for 7 days. As shown in Fig. 2D, EVs were continuously released from the scaffolds throughout the incubation period. The results indicated that scaffold stiffness plays a crucial role in the release of EVs. Scaffolds fabricated with highly methacrylated gelatin (95 %) released relatively more EVs compared to those made with lower methacrylated gelatin (50 %). Particularly, EVs-embedded scaffolds fabricated with 95 % methacrylated gelatin consistently released EVs up to day 7. In contrast, scaffolds made with 50 % methacrylated gelatin reached a steady-state release by day 5. These findings suggest that stiffer scaffolds induce prolonged EVs release. Moreover, scaffolds crosslinked with high LI released more EVs compared to those crosslinked with low LI. This may be attributed to the high light intensity producing a more stable scaffold structure, which enhances EVs embedding. Scaffolds fabricated with 95 % methacrylated gelatin and cross-linked at 75 % and 100 % LI showed substantial EVs release, with approximately 80 % of EVs released by day 7. In comparison, scaffolds cross-linked at 50 % LI released approximately 75 % of EVs within the same timeframe (Fig. 2E). These results suggest that 3D scaffolds fabricated using GelMA bioink with tunable stiffness and LI can serve as effective regulators of EVs release, holding promise for a variety of biological applications.

Optimal porosity is a crucial determinant affecting the loading capacity and release kinetics of EVs. Large-pore scaffolds facilitate the efficient incorporation of EVs into hydrogels; however, this may lead to a rapid release and ineffective EVs retention [8]. To discern the potential correlation between the physical porosity of GelMA-based scaffolds and their EVs release kinetics, we fabricated two complementary scaffolds with different filling patterns using 95 % methacrylate gelatin. One scaffold design had a 0.5-mm cubic infill grid (Fig. 3A), while the other was completely infilled (Fig. 3B). The release of EVs from both scaffolds was monitored over a 7-day period (Fig. 3C and D). Considering the different scaffold volumes, the number of released nanovesicles associated with scaffold formation was quantified and the corresponding percentages were subsequently calculated. The 0.5 mm^3 mesh grid scaffold released approximately 75 % of the total EVs, while the infilled scaffold released around 68 % (Fig. 3E and F). However, both scaffolds exhibited lower EVs release compared to the scaffold with a 0.1 mm cubic infilled mesh grid. These observations suggest that physical porosity influences EVs release, with scaffolds featuring denser porous structures facilitating a higher EVs release compared to scaffolds with larger pores or non-porous structures.

3.3. Cellular uptake of EVs and DOX in HCC-1806 TNBC cells

Combination therapy holds potential for synergistic effects in the treatment of TNBC, making it a promising therapeutic strategy. Therefore, to explore the therapeutic potential of EVs in combination with DOX and to evaluate whether the presence of EVs or DOX affects the cellular uptake of the other, we firstly assessed their respective internalization efficiencies in TNBC cells. The cells were incubated at 37°C for 24 h with either EVs alone, DOX alone, or a combination of the two treatments. Confocal microscopy analysis showed that Calcein AM-labeled EVs and DOX were efficiently internalized into TNBC cells when incubated with each component individually. The combined form, EVs+DOX, was internalized by HCC-1806 cells, with the EVs primarily localized in the cytoplasm and DOX predominantly accumulated in the nucleus (Fig. 4A). This suggests that co-administration of EVs+DOX does not interfere with DOX uptake by TNBC cells, hinting at their potential for combination therapy and possible synergistic effects. Fig. 4B shows the fluorescence profiles of cellular uptake by HCC-1806 cells under three different therapeutic agent compositions (EV alone, DOX alone, and EVs+DOX).

3.4. Cytotoxicity and ROS production in 3D TNBC model

To investigate the behavior of the chemotherapeutic drug DOX in a 3D culture system of TNBC cells, we bioprinted a 3D model in Matrigel. The 3D model culture mirrors the tumor's environment in the body and reflect the chemotherapy drug doses required to successful treatment of cancer patients. After 24 h of bioprinting, TNBC models were treated with increasing concentrations of DOX (ranging from 0.125 to 6 μM) and incubated for 48 h. The response of 3D cells to DOX in the 3D culture system revealed that cell density in the DOX-treated group was significantly lower than that of the untreated control group ((-) DOX) (Fig. 5A). A dose-dependent DOX-induced cytotoxicity was observed in 3D cultured HCC-1806 cells (Fig. 5B), with the IC50 value of DOX against the 3D TNBC model determined to be 0.344 μg/mL (Fig. 5C). Increased ROS levels were identified as an early event in DOX-induced cell death [25]. To examine the effects of DOX on intracellular ROS formation, we used a fluorinated derivative of 2′,7′-dichlorofluorescein as a fluorescent probe. As shown in Fig. 5D, elevated levels of DOX-induced ROS were detected in HCC-1806 3D models in a dose-dependent manner, correlating with decreased cell viability.

While many patients with TNBC experience months or even years of being cancer-free post-surgery, they exhibit higher recurrence rates

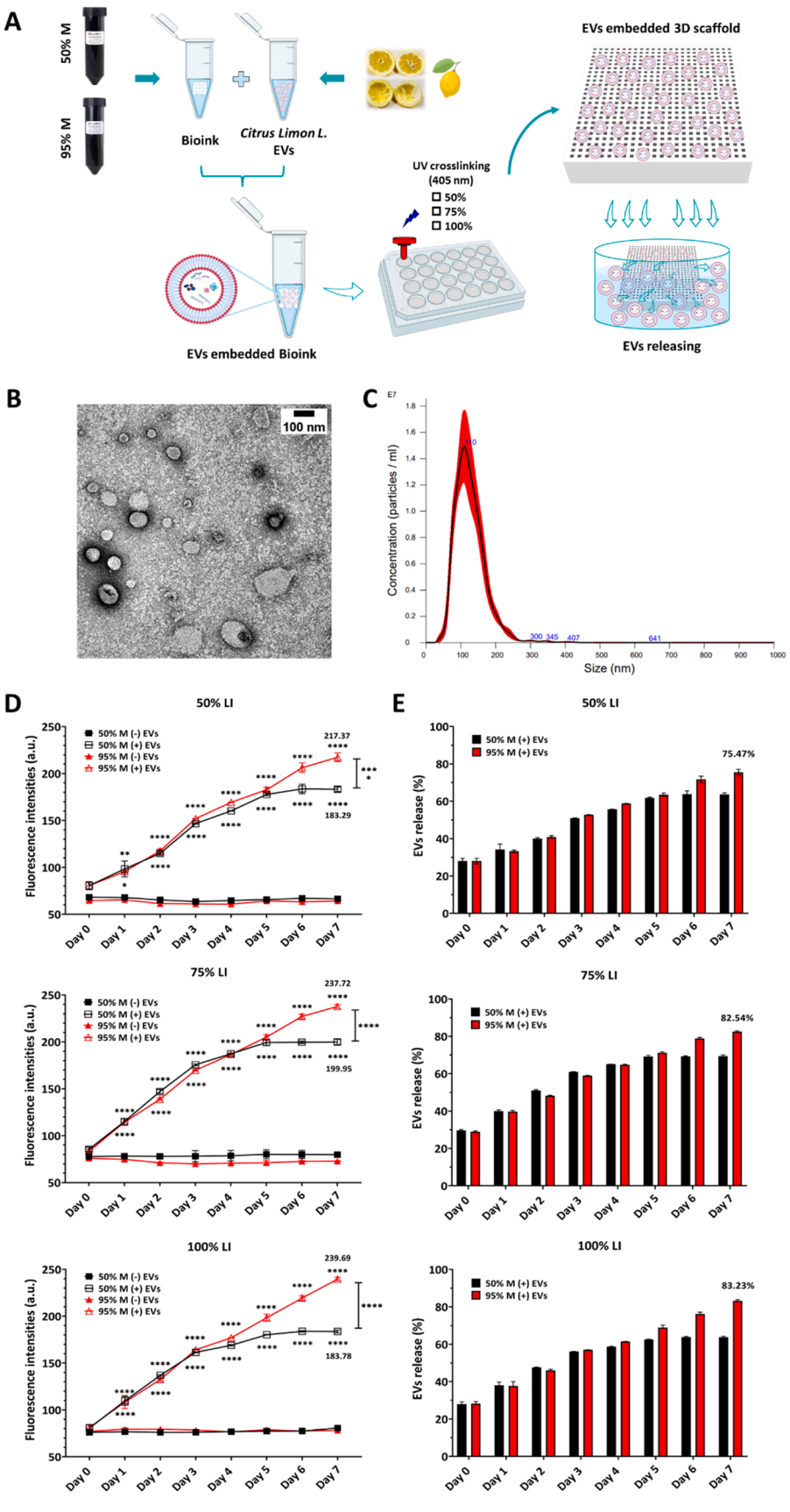

(caption on next page)

Fig. 2. Cumulative release profiles EVs from 3D EVs-embedded scaffolds. **(A)** Schematic diagram of the experimental procedure. **(B)** Representative transmission electron microscopy (TEM) image of EVs (Scale bar = 100 nm). **(C)** Size distribution and concentration of EVs determined by the nanoparticle tracking analysis (NTA). **(D)** EVs release profiles of two different degrees of methacrylated gelatin scaffolds cross-linked with 50 %, 75 %, and 100 % LI, respectively. **(E)** Percentage of EVs released from the scaffolds. Fluorescence intensities were measured by Cytation 3 Cell Imaging Multi-Mode Reader (BioTek, Winooski, VT, USA). Columns, mean ± SEM. Statistical significance was evaluated using two-way ANOVA followed by Tukey's post-hoc tests (* $p<0.05$; ** $p<0.01$; ***$p < 0.001$; ****$p < 0.0001$).

compared to patients with other BC subtypes [26]. Combination treatment approaches may synergistically enhance the overall effect of treatment. We combined the EVs scaffold patch with the widely used DOX chemotherapeutic drug to achieve local release of EVs from the 3D micropatterned patch to the tumor site after surgery, alongside systemic delivery of DOX (Fig. 6A). This dual-delivery system synergistically enhanced the anti-cancer efficacy against TNBC in 3D models, potentially mitigating tumor recurrence. 3D HCC-1806 cells were bioprinted in Matrigel, and the patches embedded without EVs (S (-) EVs), with EVs (S (-) EVs), IC50 of DOX ((+) DOX), or IC50 of DOX in combination with scaffold-embedded EVs (S (+) EVs (+) DOX), were administered to the TNBC model to evaluate their synergistic effects in the 3D culture system. Cell growth in 3D cultures was monitored over 48 h post-treatment (Fig. 6B). 3D cells treated with S (+) EVs, (+) DOX and S (+) EVs (+) DOX exhibited statistically significant cytotoxic effects with respect to the control (Ctrl) (Fig. 6C). The group of 3D cells treated with the combination strategy, S (+) EVs (+) DOX, exhibited approximately 30 % viability. This represents a 10 % decrease in viability compared to the group of cells treated with DOX alone and a 60 % decrease compared to treatment with S (+) EVs alone, highlighting the enhanced cytotoxic effect of the combined treatment regimen. Consistent with the cell viability results, the 3D TNBC model treated with S (+) EVs (+) DOX showed the highest levels of ROS production. This observation is notable, as it showed significantly higher ROS levels compared to those in cells treated solely with (+) DOX or S (+) EVs (Fig. 6D).

Next, to evaluate the long-term efficacy of co-administration of S (+) EVs and (+) DOX in the 3D TNBC model, we extended the incubation period to 7 days. The aggregation and migration behaviors of the 3D models that untreated (Ctrl) or treated with S (-) EVs, S (+) EVs, (+) DOX, or S (+) EVs (+) DOX were monitored from Day 0 to Day 7 (Fig. 7A). The cytotoxic effects on the 3D cells treated with S (+) EVs showed 80 % viability compared to the control. In the groups treated with (+) DOX and S (+) EVs (+) DOX, the cell viability was 8.6 % and 6.1 %, respectively. Compared to the 48-h incubation period, these values represent a 30 % and 20 % decrease in viability, demonstrating enhanced long-term efficacy of treatment in the 3D TNBC model (Fig. 7B). After 7 days of treatment, the groups of cells treated with S (+) EVs, (+) DOX, and the combination form S (+) EVs (+) DOX exhibited higher ROS levels compared to those observed after 48 h of treatment (Fig. 7C). Increased ROS levels over time indicate sustained oxidative stress, highlighting the long-term effects of treatments on the 3D cellular environment. In our observations, we found distinct patterns in how cells behaved under different treatments. Untreated cells (Ctrl) and those treated with S (-) EVs or S (+) EVs showed obvious aggregation and migration tendencies. Interestingly, cells treated with (+) DOX and S (+) EVs (+) DOX exhibited well-controlled cell migration (Fig. 7D). The core cell density was significantly reduced by approximately 60 % in the groups treated with (+) DOX and S (+) EVs (+) DOX compared to the Ctrl. In contrast, no significant differences were observed in the groups administered S (-) EVs or S (+) EVs relative to the control group (Fig. 7E). The obtained results indicated that S (+) EVs (+) DOX not only induced cytotoxic effects in the 3D model, evidenced by high levels of ROS production, but also significantly inhibited cell migration and aggregation laying the foundation for the design of a new treatment for metastases.

3.5. Combination therapy effectively controls cell aggregate formation and migration in an aggressive TNBC model

Metastatic tumors are responsible for more than 90 % of cancer-related deaths [27]. Even after successful surgical removal of all visible tumor cells, microscopic residual cells may persist, particularly in cases of large tumors or those that have spread to adjacent tissues or organs, posing a risk of cancer recurrence. Given that combined drug delivery approaches demonstrated remarkable anticancer effects in 3D TNBC models—significant cytotoxicity as well as inhibition of cell migration and aggregation—our goal was to evaluate their potential effectiveness in the aggressive tumor environment. The ability to accurately model and predict tumor progression, particularly the transition to a metastatic phenotype, is a critical aspect of cancer research. Traditional *in vitro* assays often fall short in replicating the complex tumor microenvironment and the dynamic processes involved in metastasis. To address these limitations, we employed a bioprinted core invasion assay to estimate tumor progression towards a metastatic phenotype on a reliable model. To enable the cells to form 3D structures that closely mimic aggressive tumor features *in vivo*, we pre-cultured them for 7 days after 3D bioprinting, to develop characteristics of aggregation and migration (Fig. 8A). The 3D cell cultures were treated starting from day 7 and were monitored until day 14 to evaluate their migration efficacy and aggregate formation (Fig. 8B). The cells bioprinted in Matrigel with a dome-shaped structure exhibited distinct migratory behaviors across different treatment groups. In the untreated group (Ctrl) and the groups treated with S (-) EVs or S (+) EVs, cells actively migrated out of Matrigel. In contrast, controlled and regulated cell migration was observed in the groups administered with (+) DOX or S (+) EVs (+) DOX. The cell density across the entire spread area is expressed as a percentage (Fig. 8C). In the core area, the cell density was significantly lower in the groups treated with (+) DOX and S (+) EVs (+) DOX compared with the other three groups that were untreated (Ctrl) or treated with S (-) EVs or S (+) EVs (Fig. 8D). As the cells migrated out of the core, the anticancer efficacy in terms of cell evasion and cell density in evaded areas was analyzed. The group receiving (+) DOX and S (+) EVs (+) DOX exhibited significantly lower cell densities compared to the other groups, with the lowest cell density observed in the group treated with S (+) EVs (+) DOX (Fig. 8E). These observations demonstrate that this combination therapy can effectively inhibit cell proliferation and migration in an aggressive 3D tumor model, highlighting its potential as a promising therapeutic strategy for both primary and metastatic tumors.

3.6. EVs-embedded scaffolds accelerate fibroblast proliferation, inhibit TNBC cell growth and promote wound closure

For the treatment of post-operative tumors, in addition to anti-tumor and anti-metastasis, strong tissue repair ability is of great significance to the health of patients. We explored the bioactivity of the scaffolds in the absence (-) or presence (+) of EVs. Fig. 9A illustrates a schematic diagram depicting the adhesion efficacy of fibroblasts and HCC-1806 cells to EVs-embedded scaffolds (S (+) EVs). Representative fluorescence images of Calcein AM-labeled EVs and DAPI-labeled nuclei are shown in Fig. 9B. Following 48 h of incubation, fibroblasts showed a higher propensity to adhere to S (+) EVs compared to EVs-free scaffolds (S (-) EVs). Conversely, HCC-1806 cells exhibited resistance to adherence to S (+) EVs, resulting in a lower number of HCC-1806 cells adhering to the scaffolds in the presence of S (+) EVs relative to S (-) EVs (Fig. 9C).

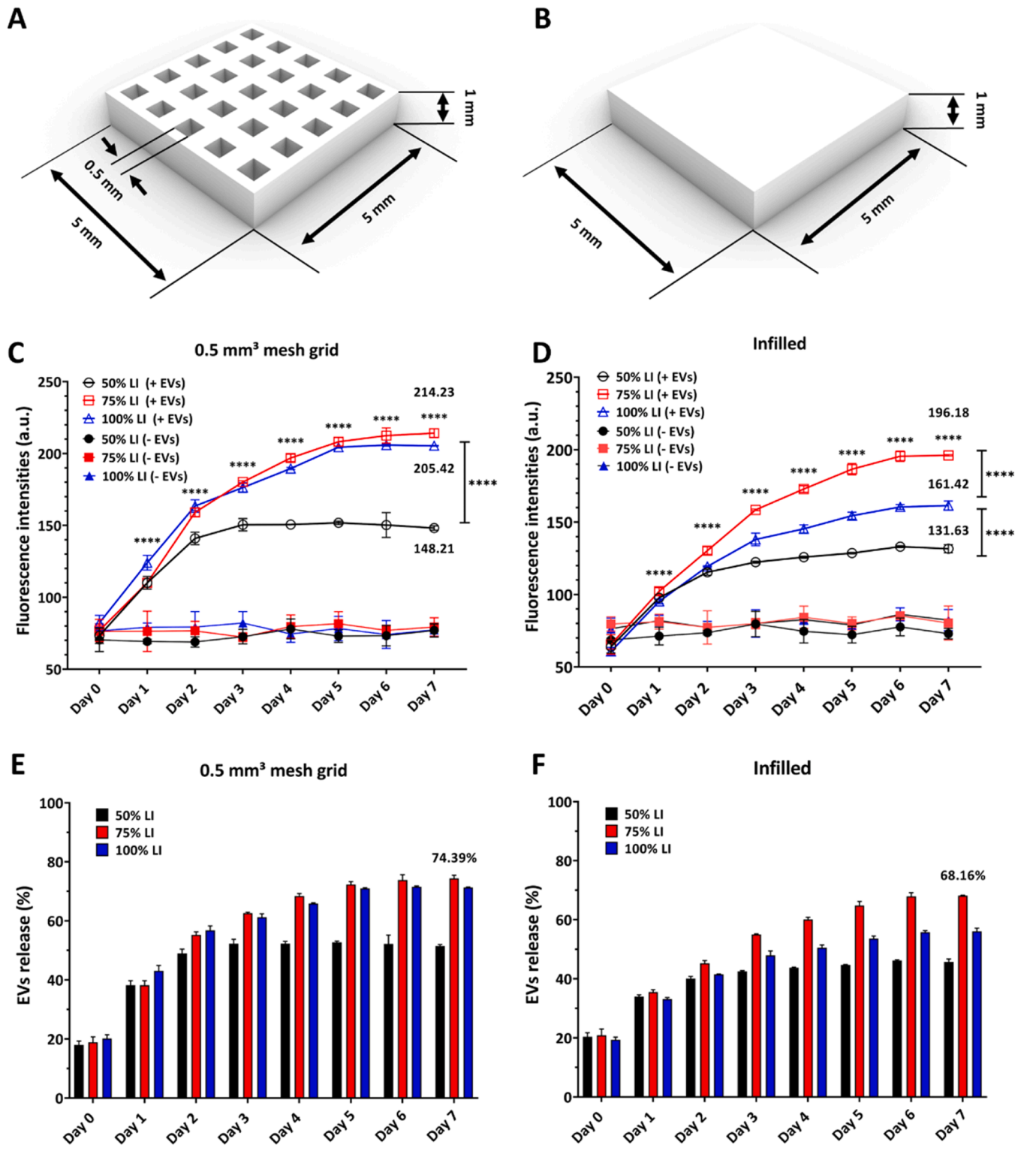

Fig. 3. EVs release from 3D scaffolds was affected by physical porosity and cross-linking UV light intensity. The scaffolds designed with **(A)** 0.5 mm^3 mesh grid and **(B)** infilled patterns of scaffold. The release profiles of EVs from **(C)** 0.5 mm^3 mesh grid and **(D)** infilled scaffolds were monitored up to day 7. Percentages of the released EVs from **(E)** 0.5 mm^3 mesh grid and **(F)** infilled scaffolds as a percentage of the total EVs. The fluorescence intensities were detected by using Cytation 3 Cell Imaging Multi-Mode Reader (BioTek, Winooski, VT, USA). Columns, Mean ± SEM. Statistical analysis was performed two-way ANOVA followed by Tukey's post-hoc tests (* $p<0.05$; ** $p<0.01$; ***$p < 0.001$; ****$p < 0.0001$).

Moreover, S (+) EVs displayed excellent biocompatibility in human fibroblasts, significantly enhancing their proliferation without inducing cytotoxic effects. In contrast, cytotoxic effects were observed in HCC-1806 cells after seeding onto S (+) EVs compared to cells seeded on S (-) EVs (Fig. 9D). These findings highlight the nontoxic nature of the scaffolds, demonstrating their safety for human fibroblasts. Notably, they enhanced fibroblast proliferation while inhibiting the growth of TNBC HCC-1806 cells, indicating their potential as a promising strategy

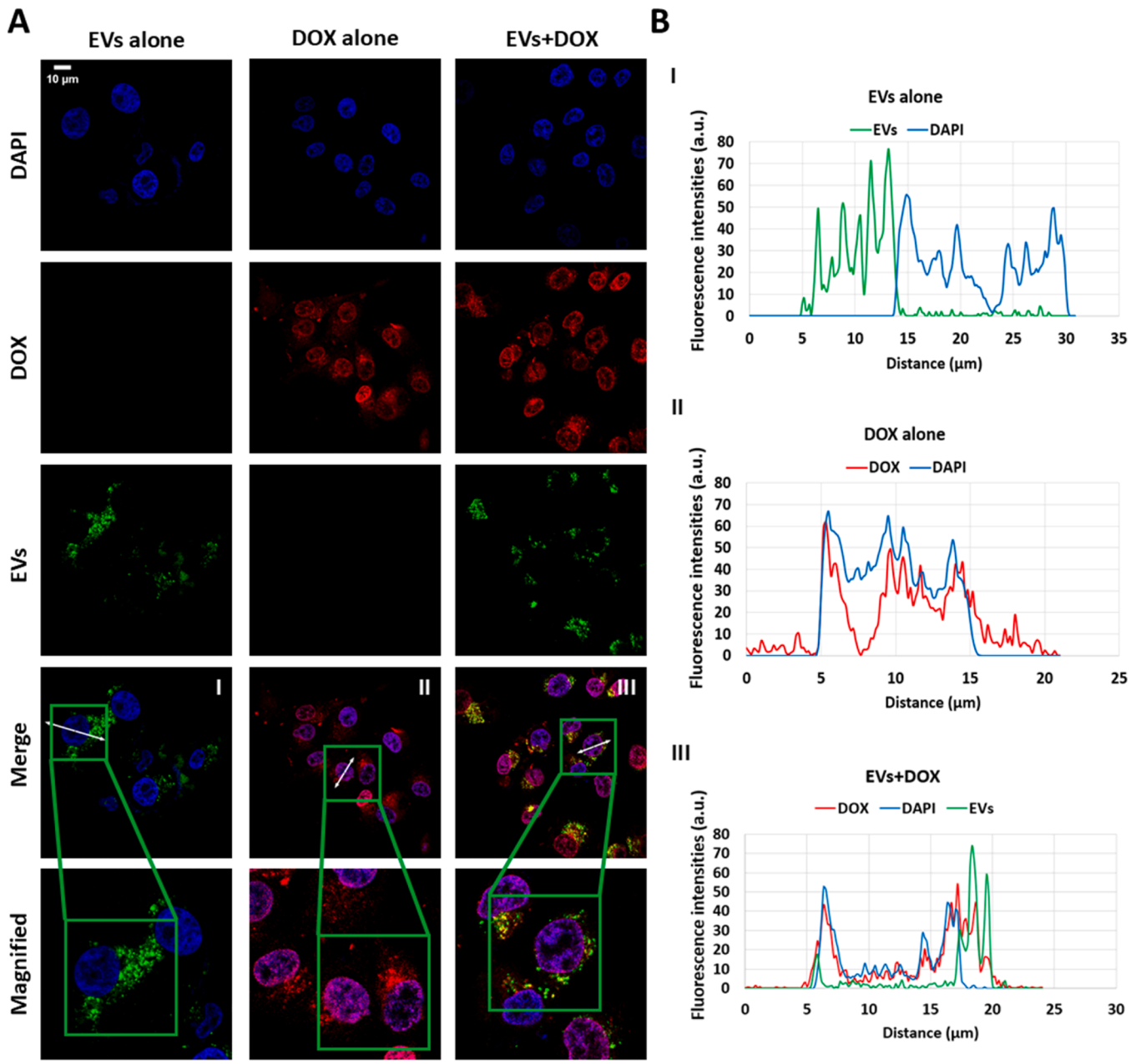

Fig. 4. Cellular uptake of EVs alone, DOX alone, and EVs+DOX in HCC-1806 cells. **(A)** Representative images of HCC-1806 cells incubated with EVs alone, DOX alone, or co-incubated with EVs+DOX at 37°C for 24 h. The EVs were labeled with Calcein-AM (shown in green), while the cell nuclei were counterstained with 4′,6-diamidino-2-phenylindole (DAPI) (scale bar = 10 μm). The magnified images depict high-magnification views of the green boxed areas. **(B)** The fluorescence spectrum of HCC-1806 cells drawn along the white arrows were analyzed by ImageJ software.

for anti-cancer therapy.

We then tested EVs-embedded scaffold ability to promote wound healing in 48 h. Fig. 10A shows representative images of wound closure in fibroblasts monolayers after administration of S (-) EVs, S (+) EVs, or no treatment (Ctrl). After a 24-h incubation period, fibroblasts treated with S (+) EVs exhibited significantly enhanced migratory behavior toward wound area compared to those treated with S (-) EVs or the control group (Fig. 10B). This effect was even more pronounced after a 48-h incubation period. In the group treated with S (+) EVs, the wound area was nearly closed, whereas the healing rate of the wound area was lower in the Ctrl and S (-) EVs group (Fig. 10C). These results indicate that EVs released from scaffolds can accelerate wound healing in fibroblasts, suggesting that scaffolds embedded with EVs have tissue regenerative capacity, which may be beneficial for wound healing after surgery.

4. Discussion

The hydrogel-based drug delivery systems have emerged as a promising strategy for improving the efficacy of chemotherapy, by reducing toxicity and side effects, also contributed to repairing the healthy tissues. Drug-loaded hydrogels can be administered to the tumor site or cavity after surgical resection of solid tumors to maintain local drug concentrations over a prolonged period of time, thereby significantly reducing the possibility of recurrence due to residual cancer cells [28]. Photo-crosslinkable hydrogels has been explored in various biomedical applications, including wound healing, drug delivery, tissue regeneration [29], organ-on-a-chip and biosensor [30]. Mi et al.

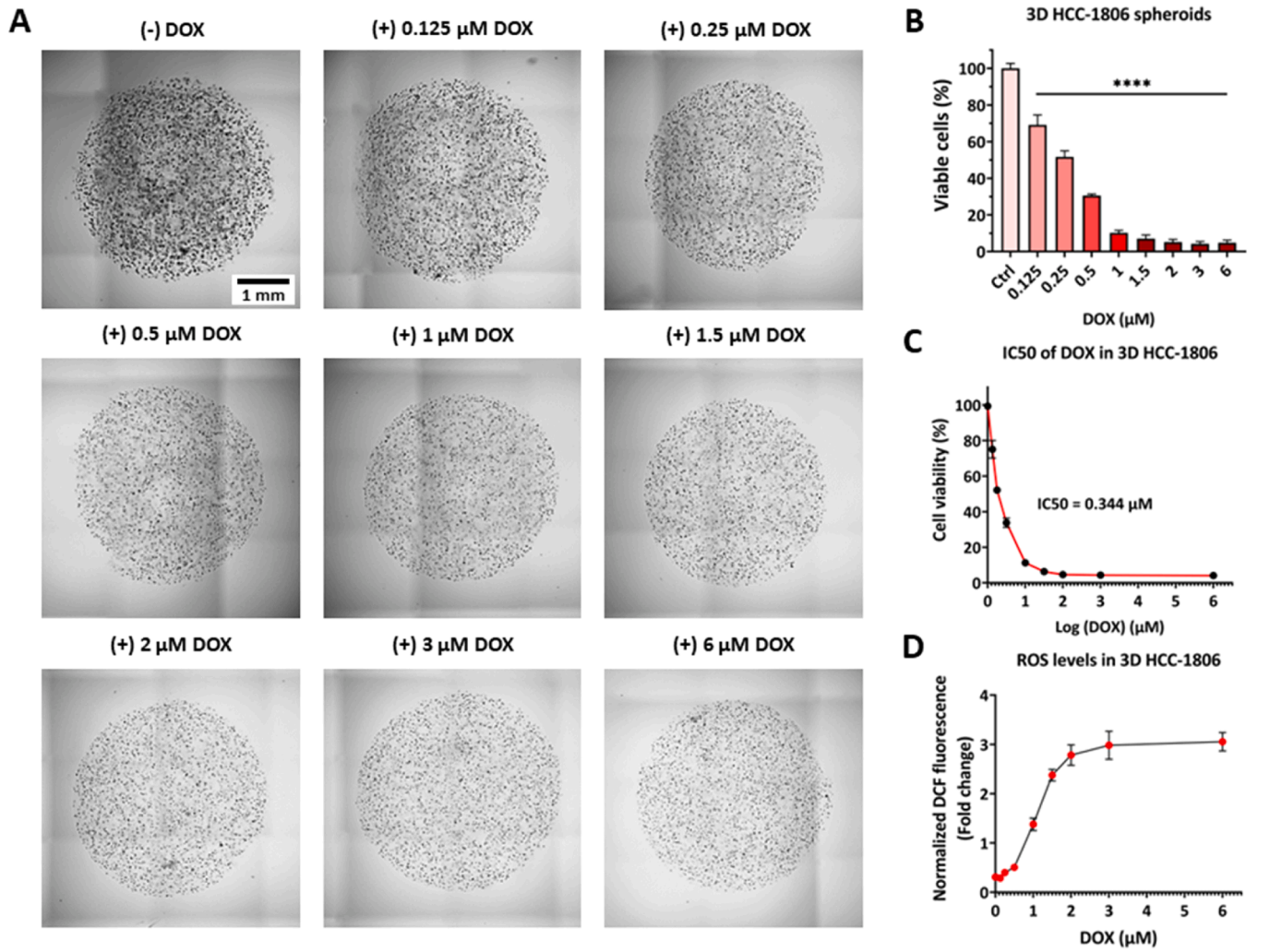

Fig. 5. Cytotoxic effects of DOX on 3D TNBC model. **(A)** Representative stitched microscopic images of 3D TNBC model after 48 h of treatment with increasing concentrations of DOX (Scale bar = 1 mm). **(B)** Dose-dependent cytotoxicity of DOX on 3D HCC-1806 cells. **(C)** IC50 of DOX against HCC-1806 cells in the 3D TNBC model. **(D)** Effect of DOX on ROS production in 3D HCC-1806 cells analyzed by H_2DCFDA after 48 h of treatment. Bars, mean ± SEM. Statistical significance was evaluated using one-way ANOVA followed by Tukey's post hoc tests (*p < 0.05; **p < 0.01; ***p < 0.001; ****p < 0.0001).

developed a photopolymerizable hydrogel incorporating DNA methyltransferase and a chemotherapeutic drug. This approach effectively filled the resection cavity, consequently preventing recurrence of TNBC in an orthotopic 4T1 breast cancer resection model [31]. The sustained release of the drug subsequently reduces the dosage required, thereby reducing overall side effects.

In this study, we fabricated EVs-embedded 3D-printed GelMA scaffolds and examined their potential for postoperative treatment of TNBC. GelMA scaffolds, known for their excellent biocompatibility and structural versatility, were combined with EVs to create a localized delivery system designed to enhance the therapeutic effect on residual tumor cells after surgical resection. 3D bioprinting of EVs-embedded scaffolds was achieved using a combination of 95 % of methacrylated gelatin bioinks, resulting in structures with distinct mechanical properties as determined by atomic force microscopy (AFM). The controlled release profile of EVs from the scaffolds over seven days is particularly promising for sustained therapeutic applications, ensuring a steady supply of bioactive vesicles to the target site, which is critical for long-term maintenance of therapeutic efficacy. The physical properties of scaffolds, including porosity and UV-crosslinking intensity, significantly affect the release profile of EVs. A denser porous structure is beneficial for increasing the release rate of EVs. In cell adhesion experiments, EVs-embedded scaffolds demonstrated excellent biocompatibility with human fibroblasts, as cells exhibited a greater tendency to attach to EVs-incorporated scaffolds, emphasizing their non-toxic properties. This was further evidenced by a wound healing assay, which showed a marked increase in wound closure in the presence of EVs scaffolds. In HCC-1806 cells, the propensity to attach to EVs-embedded scaffolds was reduced compared to scaffolds alone. Notably, EVs-embedded scaffolds promoted fibroblast proliferation while inhibiting cancer cell proliferation. This dual functionality is promising for the development of therapies that target cancer cells while supporting normal tissue regeneration, potentially improving postoperative recovery outcomes for patients.

Furthermore, we employed human TNBC cells to create 3D bioprinted models, which more accurately mimic the physiological environment of the human body compared to traditional animal models, such as mice. These 3D models provide a more representative platform for studying human cellular behavior and the tumor microenvironment, enhancing the precision of our investigation into the therapeutic potential of the dual-delivery system. The combination of the EVs scaffold with the chemotherapeutic agent DOX revealed a synergistic effect in the 3D TNBC model. This combination takes advantage of the unique properties of both therapeutics. *Citrus limon L.*, commonly known as lemon, is rich in bioactive compounds, including EVs that can be used for therapeutic purposes, exhibit anti-inflammatory, antioxidant, and regenerative properties [32]. The natural origin and biocompatibility of

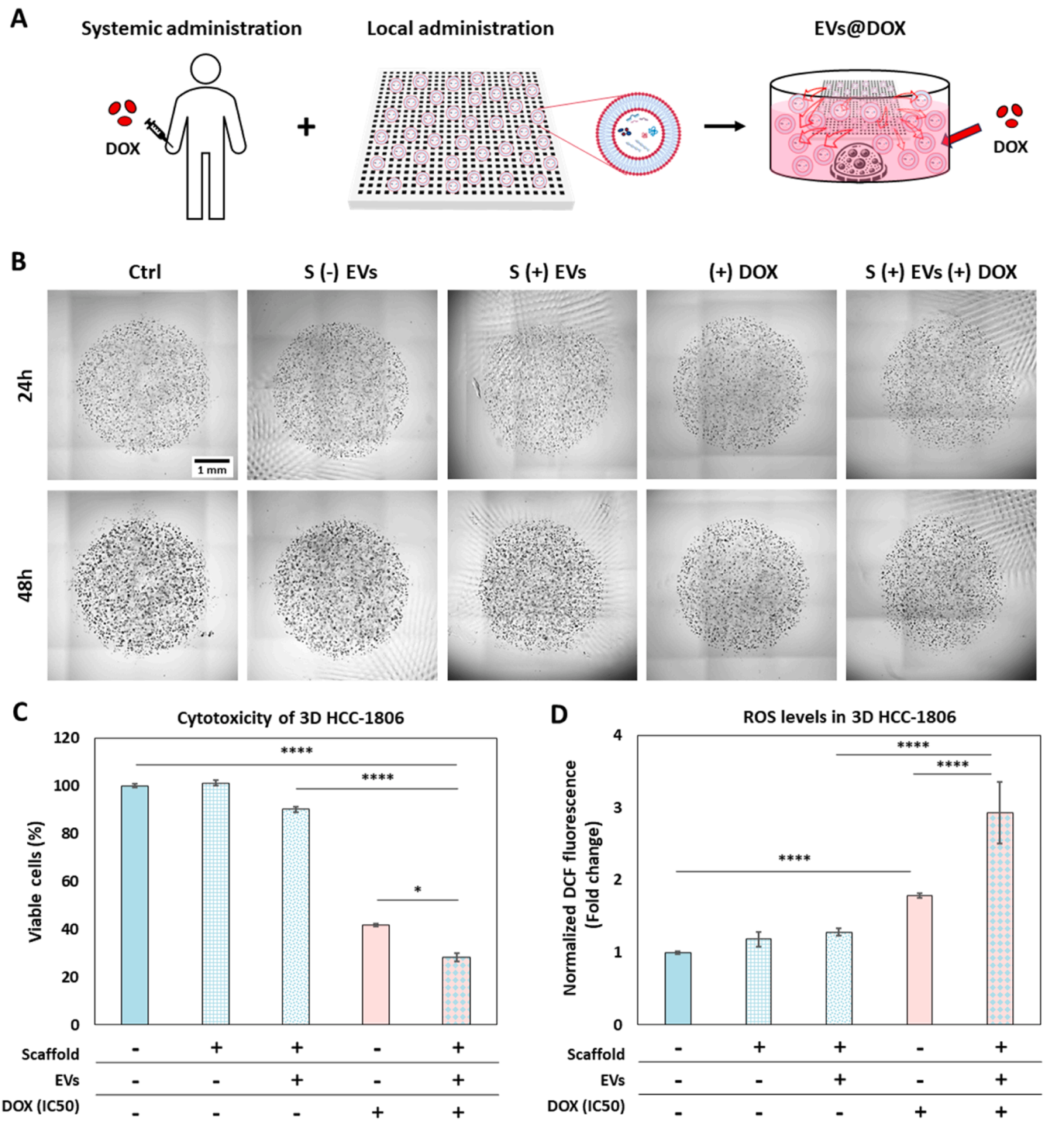

Fig. 6. The combination of EVs patch with DOX synergistically enhances the anti-cancer effect in 3D TNBC model. **(A)** Schematic illustration of the combinatorial strategy of the experimental scheme. **(B)** Representative stitched microscopic images of 3D TNBC cells following 48-h incubation without (Ctrl) or with S (-) EVs, S (+) EVs, IC50 of DOX ((+) DOX), or IC50 of DOX in combination with EVs (S (+) EVs (+) DOX) (Scale bar = 1 mm). IC50 of DOX = 0.344 μg/mL. **(C)** Cell viability of 3D HCC-1806 cells after 48 h incubation. The results were expressed as the percentage of viable cells with respect to the control (Ctrl). **(D)** After 48 h of treatment, ROS generation in 3D HCC-1806 cells was measured by H_2DCFDA staining. Bars, mean ± SEM. Statistical significance was evaluated using one-way ANOVA followed by Tukey's post hoc tests (*$p < 0.05$; **$p < 0.01$; ***$p < 0.001$; ****$p < 0.0001$).

Citrus limon L. EVs make them suitable for integration into biomedical platforms, enhancing the efficacy of therapeutic agents. DOX, a potent chemotherapeutic agent, is widely used in systemic treatment due to its effectiveness against various cancers, including TNBC. The combination regimen exhibited the highest levels of ROS production after 48 h and 7 days of incubation, indicating enhanced oxidative stress and cytotoxicity compared with either treatment alone and showing long-term efficacy in both primary and metastatic TNBC models. Controlled migration and reduced core cell density in the model tumor progression towards a metastatic phenotype further support the efficacy of this combination therapy in replicating the complex tumor microenvironment and the dynamic processes involved in metastasis. This

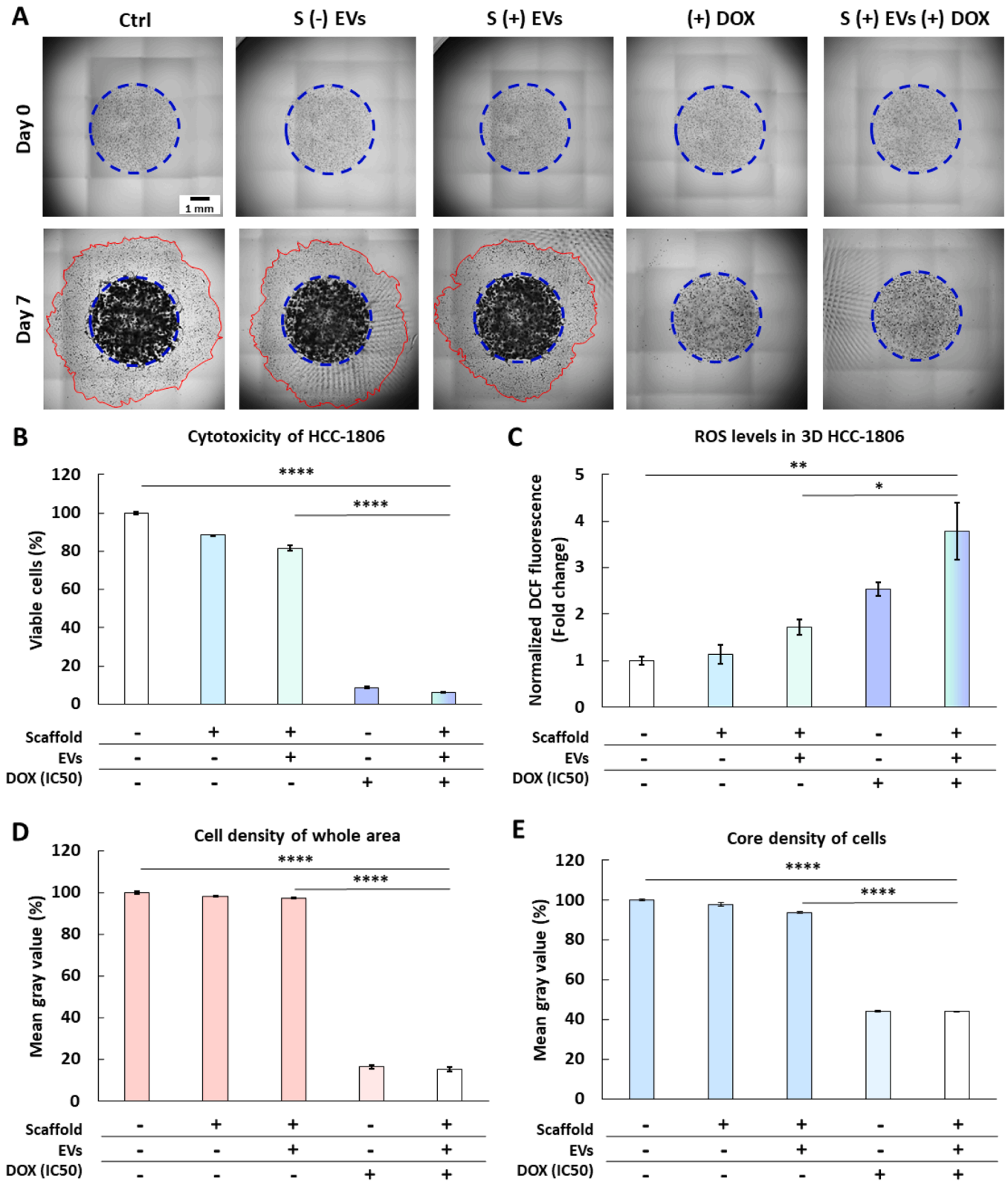

Fig. 7. Long-term efficiency of co-administration of S (+) EVs and (+) DOX in the 3D TNBC model. **(A)** Representative stitched microscopic images of 3D TNBC cells following 7 days incubation without (Ctrl) or with S (-) EVs, S (+) EVs, (+) DOX, or S (+) EVs (+) DOX. In the images, blue dashed circles indicate the core cell density, whereas red irregular circles outline the edges of migrating cells (Scale bar = 1 mm). IC50 of DOX= 0.344 μg/mL. **(B)** Cell viability of 3D HCC-1806 cells after 7 days of incubation. The results were expressed as the percentage of viable cells with respect to the control (Ctrl). **(C)** After 7 days of treatment, ROS generation in 3D HCC-1806 cells was measured by H_2DCFDA staining. **(D)** Core cell density (%) on day 7 after treatment. **(E)** Core cell density (%) on day 7 after treatment. Bars, mean ± SEM. Data from three independent experiments performed in triplicate were analyzed by ImageJ software. Statistical significance was evaluated using one-way ANOVA followed by Tukey's post hoc tests (*$p < 0.05$; **$p < 0.01$; ***$p < 0.001$; ****$p < 0.0001$).

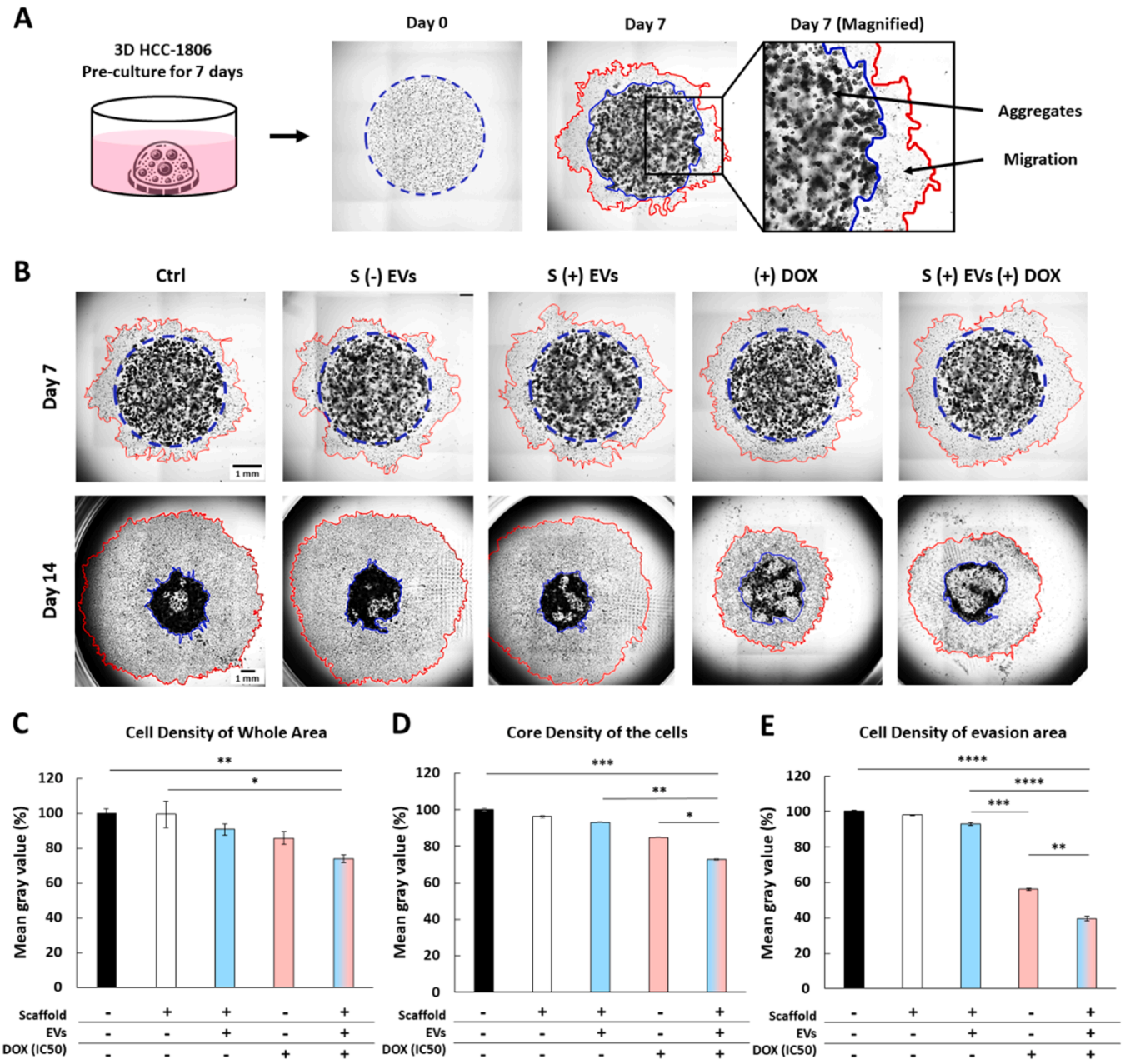

Fig. 8. Anticancer effects of the S (+) EVs (+) DOX combination approach in an invasive TNBC model. **(A)** 3D HCC-1806 cells pre-cultured for 7 days to develop the invasive TNBC model. **(B)** Representative stitched microscopic images of 3D HCC-1806 cells were acquired on day 7 and day 14 in the absence or presence of S (-) EVs, S (+) EVs, IC50 of DOX, or S (+) EVs (+) DOX (Scale bar = 1 mm). IC50 of DOX = 0.344 μg/mL. In the images, blue dashed circles indicate the core cell density, whereas red irregular circles outline the edges of migrating cells. **(C)** Cell density (%) of the whole area on day 14 after incubation. **(D)** Core cell density (%) on day 14 after treatment. **(E)** Cell density (%) in the evasion area on day 14. Bars, mean ± SEM. Data from three independent experiments performed in triplicate were analyzed by ImageJ software. Statistical significance was evaluated using one-way ANOVA followed by Tukey's post hoc tests (*$p < 0.05$; **$p < 0.01$; ***$p < 0.001$; ****$p < 0.0001$).

synergistic effect highlights the potential of using EVs scaffolds to improve the target delivery and effectiveness of traditional chemotherapeutic drugs.

This study presents a novel approach to TNBC treatment and tissue regeneration by combining the unique properties of *Citrus limon L.*-derived EVs with advanced 3D bioprinting technology. The dual-delivery system, consisting of a 3D-bioprinted GelMA hydrogel scaffold patch embedded with EVs and combined with DOX, significantly enhances the anti-cancer effects compared to using either EVs or DOX alone. The EVs-embedded scaffold offers a sustained and localized treatment modality, potentiates the anti-cancer effects of DOX, and maintains a supportive microenvironment for healthy tissue regeneration. This approach could potentially reduce tumor recurrence and improve patient outcomes, offering a promising platform for future biomedical applications.

5. Conclusion

The novel strategy of combining controlled release of natural *Citrus limon L.*-derived EVs from 3D GelMA scaffolds with DOX presents a promising approach to inhibit TNBC. This dual-delivery system effectively targets both local and systemic delivery by using bioprinted scaffolds to achieve local and sustained delivery of EVs and systemic delivery of the chemotherapeutic agent DOX. The biocompatibility and

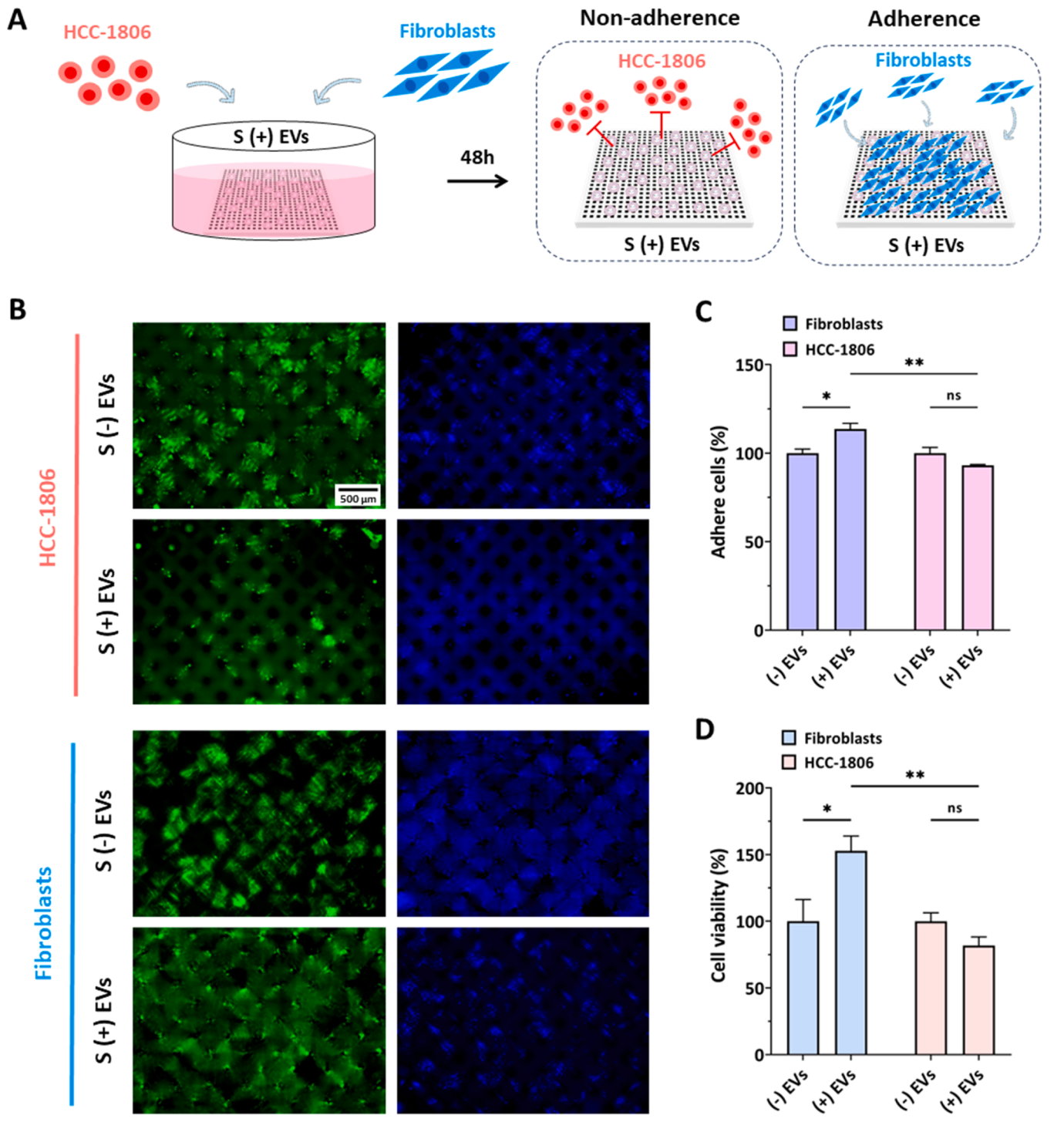

Fig. 9. Proliferation and adhesion efficiency of human fibroblasts and HCC-1806 cells on EVs-embedded scaffolds. **(A)** Schematic diagram of the workflow for analyzing cell adhesion efficiency on EVs-embedded scaffolds (S (+) EVs) (Scale bar = 500 μm). **(B)** Representative fluorescence images of live cells and nuclei on scaffolds (S) in the absence (-) or presence (+) of EVs after 48 h of incubation. Live cells were stained with Calcein-AM (green fluorescence), and nuclei were stained with DAPI (blue fluorescence). **(C)** Adhesion efficacy of fibroblasts and HCC-1806 cells to S (-) EVs and S (+) EVs. **(D)** Cell viability of fibroblasts and HCC-1806 cells on S (-) EVs and S (+) EVs. Columns, mean ± SEM. Statistical significance was evaluated using two-way ANOVA followed by Tukey's post hoc tests (*$p < 0.05$; **$p < 0.01$).

mechanical stability of the GelMA scaffolds, along with the sustained release profile of the EVs, contribute to the effectiveness of this dual-delivery system. Overall, this combination therapy elicited synergistic effect, significantly reducing TNBC cell viability, aggregation, and migration in both primary and metastatic TNBC models, representing a highly effective strategy against this aggressive cancer subtype that could reduce side effects in TNBC treatment and improve patient outcomes.

Ethics statement

Ethical approval was not required for this study in accordance with

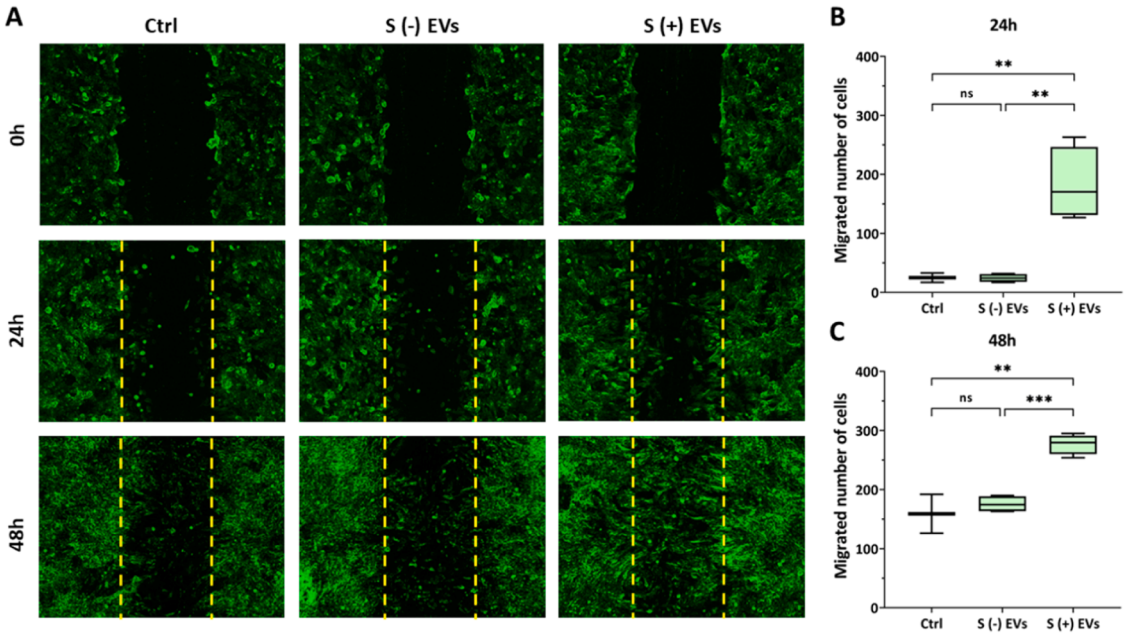

Fig. 10. EVs-embedded scaffolds accelerate fibroblast wound closure. Wound healing assays were performed on fibroblasts subjected to scratch wounds and treated with either no treatment (Ctrl), scaffolds without EVs (S (-) EVs), or scaffolds with EVs (S (+) EVs). **(A)** Representative images showing cell migration into the wound area after treatment. The number of migrated cells following 24 h **(B)** and 48 h **(C)** of incubation. Graphical representation of data from three independent experiments performed in triplicate analyzed by ImageJ software. Bars, mean ± SEM. Statistical significance was evaluated using one-way ANOVA followed by Tukey's post hoc tests (*$p < 0.05$; **$p < 0.01$; ***$p < 0.001$).

the local legislation and institutional requirements because only commercially available established cell lines were used.

CRediT authorship contribution statement

Lishan Cui: Writing – original draft, Methodology, Investigation, Formal analysis, Data curation, Conceptualization. **Giordano Perini:** Writing – review & editing, Validation, Supervision, Methodology, Formal analysis, Data curation. **Antonio Minopoli:** Methodology, Formal analysis, Data curation. **Alberto Augello:** Resources, Methodology, Investigation. **Marco De Spirito:** Writing – review & editing, Supervision, Software, Resources. **Valentina Palmieri:** Writing – review & editing, Visualization, Supervision, Resources, Project administration. **Massimiliano Papi:** Writing – review & editing, Validation, Supervision, Resources, Project administration, Conceptualization.

Declaration of Competing Interest

The authors declare the following financial interests/personal relationships which may be considered as potential competing interests: Lishan Cui reports financial support was provided by Fondazione Umberto Veronesi Postdoctoral Fellowships Grant 2024. Valentina Palmieri reports financial support was provided by European Union - NextGenerationEU. If there are other authors, they declare that they have no known competing financial interests or personal relationships that could have appeared to influence the work reported in this paper.

Acknowledgments

This work was supported by the Fondazione Umberto Veronesi (Postdoctoral Fellowships Grant 2024 to LC). We would like to acknowledge the contribution of 3D Bioprinting Research Core Facility G-STeP and Microscopy Research Core Facility G-STeP of the Fondazione Policlinico Universitario "A. Gemelli" IRCCS for sample processing. VP acknowledges Project PNC 0000001 D3 4 Health Digital Driven Diagnostics, prognostics and therapeutics for sustainable Health care, CUP B53C22006100001, The National Plan for Complementary Investments to the NRRP, Funded by the European Union - NextGenerationEU". Università Cattolica del Sacro Cuore contributed to the funding of this research project and its publication (Linea D3.2).

Data Availability

The original contributions presented in the study are included in the article/Supplementary Material, further inquiries can be directed to the corresponding authors.

References

[1] L. Yin, et al., Triple-negative breast cancer molecular subtyping and treatment progress, Breast Cancer Res. 22 (1) (2020) 61.
[2] S. Dębska-Szmich, P. Potemski, Systemic treatment in triple-negative breast cancer patients — standard and novel approaches. Oncol. Clin. Pract. (2023). **0**(0).
[3] K.R. Pawloski, A.V. Barrio, Breast surgery after neoadjuvant systemic therapy, Transl. Breast Cancer Res. 5 (2024) 13.
[4] T.C. Ho, et al., Hydrogels: properties and applications in biomedicine, Molecules 27 (9) (2022).
[5] H. Zhang, et al., Enhanced postoperative cancer therapy by iron-based hydrogels, Biomater. Res. 26 (1) (2022) 19.
[6] R.-Z. Tang, et al., Multiple local therapeutics based on nano-hydrogel composites in breast cancer treatment, J. Mater. Chem. B 9 (6) (2021) 1521–1535.
[7] S. Bashir, et al., Fundamental concepts of hydrogels: synthesis, properties, and their applications, Polym. (Basel) 12 (11) (2020).
[8] Y. Ju, et al., Extracellular vesicle-loaded hydrogels for tissue repair and regeneration, Mater. Today Bio 18 (2023) 100522.
[9] H. Yu, et al., Stimulus-responsive hydrogels as drug delivery systems for inflammation targeted therapy, Adv. Sci. (Weinh.) 11 (1) (2024) e2306152.
[10] M.M.H. Rumon, et al., Self-healing hydrogels: development, biomedical applications, and challenges, Polymers (Basel) 14 (21) (2022).
[11] C. Zhang, et al., Highly adhesive and self-healing γ-PGA/PEDOT:PSS conductive hydrogels enabled by multiple hydrogen bonding for wearable electronics, Nano Energy 95 (2022) 106991.
[12] A. Erfani, A.E. Diaz, P.S. Doyle, Hydrogel-enabled, local administration and combinatorial delivery of immunotherapies for cancer treatment, Mater. Today 65 (2023) 227–243.
[13] S. Bupphathong, et al., Gelatin methacrylate hydrogel for tissue engineering applications-a review on material modifications, Pharmaceuticals (Basel) 15 (2) (2022).
[14] A.G. Kurian, et al., Multifunctional GelMA platforms with nanomaterials for advanced tissue therapeutics, Bioact. Mater. 8 (2022) 267–295.

[15] H. Hu, et al., miR-23a-3p-abundant small extracellular vesicles released from Gelma/nanoclay hydrogel for cartilage regeneration, J. Extra Vesicles 9 (1) (2020) 1778883.
[16] D.K. Jeppesen, et al., Extracellular vesicles and nanoparticles: emerging complexities, Trends Cell Biol. 33 (8) (2023) 667–681.
[17] M.A. Kumar, et al., Extracellular vesicles as tools and targets in therapy for diseases, Signal Transduct. Target. Ther. 9 (1) (2024) 27.
[18] L. Cui, et al., Plant-derived extracellular nanovesicles: a promising biomedical approach for effective targeting of triple negative breast cancer cells, Front. Bioeng. Biotechnol. 12 (2024).
[19] M. Nemati, et al., Plant-derived extracellular vesicles: a novel nanomedicine approach with advantages and challenges, Cell Commun. Signal. 20 (1) (2022) 69.
[20] L.Y. Lin, et al., Tumour cell-derived exosomes endow mesenchymal stromal cells with tumour-promotion capabilities, Oncogene 35 (46) (2016) 6038–6042.
[21] P.J. Mishra, et al., Carcinoma-associated fibroblast-like differentiation of human mesenchymal stem cells, Cancer Res. 68 (11) (2008) 4331–4339.
[22] G. Perini, et al., INSIDIA 2.0 high-throughput analysis of 3D cancer models: multiparametric quantification of graphene quantum dots photothermal therapy for glioblastoma and pancreatic cancer, Int. J. Mol. Sci. 23 (6) (2022) 3217.
[23] Y. Hu, et al., Cryogenic 3D printed hydrogel scaffolds loading exosomes accelerate diabetic wound healing, Chem. Eng. J. 426 (2021) 130634.
[24] H.-C. Yan, et al., The delivery of extracellular vesicles loaded in biomaterial scaffolds for bone regeneration, Front. Bioeng. Biotechnol. 8 (2020).
[25] P. Datta, et al., 3D bioprinting for reconstituting the cancer microenvironment, NPJ Precis. Oncol. 4 (1) (2020) 18.
[26] S.M. Reddy, et al., Long-term survival outcomes of triple-receptor negative breast cancer survivors who are disease free at 5 years and relationship with low hormone receptor positivity, Br. J. Cancer 118 (1) (2018) 17–23.
[27] J. Fares, et al., Molecular principles of metastasis: a hallmark of cancer revisited, Signal Transduct. Target. Ther. 5 (1) (2020) 28.
[28] M. Wang, et al., Paclitaxel-nanoparticles-loaded double network hydrogel for local treatment of breast cancer after surgical resection, Mater. Sci. Eng. C Mater. Biol. Appl. 114 (2020) 111046.
[29] X. Zhao, et al., Photocrosslinkable gelatin hydrogel for epidermal tissue engineering, Adv. Health Mater. 5 (1) (2016) 108–118.
[30] Y. Piao, et al., Biomedical applications of gelatin methacryloyl hydrogels, Eng. Regen. 2 (2021) 47–56.
[31] D. Mi, et al., Postsurgical wound management and prevention of triple-negative breast cancer recurrence with a pryoptosis-inducing, photopolymerizable hydrogel, J. Control. Release 356 (2023) 205–218.
[32] M.Q. Lian, et al., Plant-derived extracellular vesicles: recent advancements and current challenges on their use for biomedical applications, J. Extra Vesicles 11 (12) (2022) e12283.